Pressure and velocity fields decomposition around a flapping wing

Marco Raiola[1,*]

1: Aerospace Engineering Group, Universidad Carlos III de Madrid, Spain
*Corresponding author: mraiola@ing.uc3m.es

Keywords: Flapping Wings, Pressure estimation from PIV, Proper Orthogonal Decomposition, Quadratic Stochastic Estimation.

ABSTRACT

In the present work, the velocity and pressure fields around a flapping airfoil in pitching/heaving sinusoidal motion are decomposed in modes in the wing-fixed reference frame. This approach is aimed at assessing the contribution of the fluid structures forming on the wing surface to the aerodynamic forces. The velocity field used for this work have been obtained through Particle Image Velocity experiments at a chord-based Reynolds number of 3600 and a Strouhal number equal to 0.2. The pressure field has been reconstructed from the phase-average velocity fields using a finite-differences Poisson solver. Finally, the velocity and pressure fields have been interpolated on a wing-fixed domain and decomposed using Proper Orthogonal Decomposition and Quadratic Stochastic Estimation to account for the quadratic relation between velocity and pressure. The decomposition identified vortical flow structures over the wing which model the evolution of bound vorticity, as well as leading edge and trailing edge vortices, over the wing. These modes contribute linearly to the chord-normal force by interacting with the constant free stream contained in the time average, as well as quadratically to the chord-wise force.

1. Introduction

The unsteady aerodynamics of wings in flapping motion is especially relevant for the design of bio-inspired Micro Air Vehicles (MAVs) operating in a low-Reynolds-number regime, ($Re \leq O(10^4)$, Shyy et al., 2007). Natural flyers and swimmers use of flapping wings or fins to efficiently produce high lift and thrust coefficients despite operating at low Reynolds numbers (Lighthill, 1969; Ellington, 1984).

The performances of flapping wings can be ascribed to the vortices (such as the Leading Edge Vortex, LEV, and the Trailing Edge Vortex, TEV) which form on the wing surface while undergoing dynamic stall and which are periodically shed in the airfoil wake. The presence of these vortices delay the complete flow separation and allow the wing to produce additional aerodynamic forces which can improve the flight performances at low Reynolds numbers.

Forces in flapping airfoils at high Reynolds numbers (such as for the case of wing flutter) have been modelled with linear potential-flow theory assuming the small-perturbation hypothesis, as in the pioneering works of Theodorsen (1935) and Garrick (1937). The lift model includes an added-mass contribution and a circulatory contribution, including both a quasi-steady and wake-induced circulations. The drag model includes the projection of the lift and a leading-edge suction due to the LEV. While this model provides a simple link between the wing kinematics and the aerodynamic forces, its application is limited to small-angle oscillations and inviscid high-Reynolds flows.

To overcome these limitations, a quasi-steady model has been proposed by Sane & Dickinson (2002), which decomposes the chord-normal force in an added-mass force, a quasi-steady circulatory force, a force depending on the wing rotation and a force due to the wake capture. This model has been further refined by Pesavento & Wang (2004) adding a viscous force term. The modelling of the circulatory contribution, however, requires the fitting the force obtained either from experiments (Sane & Dickinson, 2002) or simulations (Pesavento & Wang, 2004) to account for dynamic stall effects. Brunton et al. (2013), instead, derived a purely data-driven force model for control purposes through Balanced Proper Orthogonal Decomposition techniques using the potential linear models as a skeleton.

Flow-based decompositions can provide a more clear link between the generation of aerodynamic forces and the velocity field structures using a data-drive approach, thus unveiling the physics of the phenomenon. Liang & Dong (2015) applied Proper Orthogonal Decomposition (POD, Berkooz et al., 1993) on the flow over a 3D flapping wing, using a POD-Galerkin projection of the Impulse Equation (see Noca et al., 1999), to determine the mode contribution to the aerodynamic force. The flow decomposition proposed by Liang & Dong (2015) was performed in the inertial reference frame, in which the wing is moving, thus not allowing to identify the effect of the flow features generated on the wing surface, but only the effecto of the ones in the wake. A more accurate decomposition of the flow over the wing requires the flow to be mapped in a reference frame in which the wing is fixed. The choice of the decomposition reference frame has been addressed by several authors, e.g. Lewin & Haj-Hariri (2005) propose to perform the POD in a wing-fixed reference frame while Troshin & Seifert (2018) propose to remap the flow domain in a steady domain using a volume-preserving transformation. Raiola et al. (2021) performed the POD decomposition in a wing-fixed reference frame. The contribution of these modes to aerodynamic forces is then extracted by applying Extended POD (i.e. a Linear Stochastic Estimation in the space spanned by the POD modes, see Borée, 2003) on force measurements from a load balance. The relation between velocity field and pressure field has been investigated in several studies using stochastic estimation techniques. Naguib et al. (2001) estimated the relation between hotwire measurements and wall-mounted microphones in a boundary layer, finding the necessity to include the quadratic term in the estimation in order to provide a proper modelling. Ausseur et al. (2006) used a time-domain Quadratic Stochastic Estimation to estimate the POD time coefficients of the measured velocity field in unsampled instant in the separated flow over an airfoil. Baars & Tinney (2014) developed a POD-based spectral Higher Order Stochastic Estimation and tested it by relating a simulated supersonic-jet pressure wavepacket with its acoustic pressure signature in the far-field.

Following Raiola et al. (2021), in this work the velocity field around a flapping airfoil, measured from a planar Particle Image Velocimetry (PIV) experiment, is decomposed using POD. The decomposition is performed in a reference frame fixed on the wing to capture the flow structure on top of the wing surface. The velocity field are used to compute the pressure field around the wing using a Poisson approach. The quadratic contribution of the velocity field modes to the pressure field is then extracted by means of Quadratic Stochastic Estimation (QSE).

2. Experimental setup

The experimental setup used in this work is the same used by Raiola et al. (2021) and it will be briefly reported here. The flow field around a flapping airfoil in sinusoidal heaving/pitching motion has been measured in the water tunnel facility of the *Universidad Carlos III de Madrid*, featuring a $2.5\,\mathrm{m} \times 0.5\,\mathrm{m} \times 0.55\,\mathrm{m}$ glass test section. An aluminum 2D wing with a NACA 0012 section and aspect ratio of 16.3 has been tested at a chord-based Reynolds number of 3600. Motion has been provided through a 4-bar linkage driven by 2 linear actuators, providing both heaving h and pitching θ motion as described in Eq. 1, in which c is the wing chord and f is the flapping frequency corresponding to a Strouhal number $St = 2cf/U_\infty = 0.2$.

$$\begin{aligned} h(t) &= c\,\sin(2\pi f t) \\ \theta(t) &= \theta_m + \theta_0\,\sin(2\pi f t + \pi/2) \end{aligned} \tag{1}$$

Planar Particle Image Velocimetry (PIV) measurements are carried out in a *x-y* plane placed at a distance of 5.5c from the tip. The flow is seeded with neutrally-buoyant polyamide particles with $56\,\mu$m diameter. The PIV system is composed by a dual-cavity Nd:Yag Quantel Evergreen laser ($200\,$mJ/pulse at $15\,$Hz) and a 5.5 Mpixels Andor sCMOS camera. PIV images resolution is about $8.5\,$pixel/mm for the present experiment. The PIV system is synchronized with the movement system providing phase-averaged measurements of 55 snapshots each for 80 different phases of the flapping motion. The PIV images background is removed via an eigenbackground removal procedure (Mendez et al., 2017). Flow fields are extracted through an iterative multi-grid/multi-pass image deformation algorithm (Scarano, 2001) with final interrogation windows of 32×32 pixels and 75% overlap. Following the typical figure of merit for PIV uncertainty provided by Westerweel (1997), the measurement error is estimated to be 0.8% of the free-stream velocity. Two separate experiments with illumination on different sides of the wing have been carried out and their phase-averaged fields have been merged in order to provide a complete map of the velocity field around the wing.

The aerodynamic force is measured with an ATI Industrial Automations Nano-17 load cell with IP68 waterproofing connected between the wing and the linkage. According to the manufacturer specification and the test conditions, the resolution of the measured force coefficients is estimated to be 0.03. Signal detrending is applied to remove the load cell long-period thermal drift and a

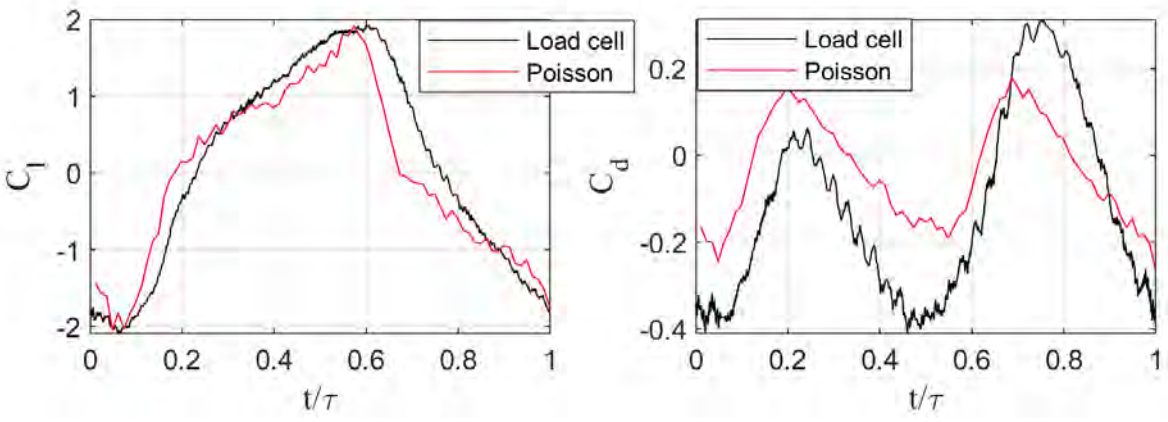

Figure 1. Lift (C_l) and drag (C_d) coefficients for the case with $\theta_m = 10°$ and $\theta_0 = 10°$ measured with the load cell and estimated from the Poisson equation.

low pass filter with threshold at $St = 5$ is applied to remove electromagnetic noise. Force measurements are phase-averaged and corrected for the wing inertia force and for the waterproofing-induced height-dependent bias, both determined experimentally. The final uncertainty on the force coefficients is estimated experimentally to be lower than 0.1.

Pressure fields are estimated from the measured velocity fields by means of the Poisson equation (Van Oudheusden, 2013) resulting from the divergence of the incompressible Navier-Stokes equation (Eq. 2), is which p is the pressure field, $\mathbf{u}$ is the velocity field and ρ is the fluid density.

$$\nabla^2 p = -\rho \nabla \cdot (\mathbf{u} \cdot \nabla)\mathbf{u} \tag{2}$$

A Matlab-based finite-differences scheme has been implemented, based on the work of Reimer & Cheviakov (2013), supporting mixed Dirichlet and Neumann type boundary conditions. Dirichlet conditions with pressure equivalent to null have been imposed on the upwind, upper and lower boundaries of the domain. Non-homogeneous Neumann conditions have been applied on the downwind boundary as well as on the wing surface. The Neumann conditions have been derived directly from the Navier-Stokes equation (Eq. 3), in which D/Dt stands for the material derivative and μ is the fluid viscosity.

$$\nabla p = \mathbf{f}(\mathbf{u}) = -\rho \frac{D\mathbf{u}}{Dt} + \mu \nabla^2 \mathbf{u} \tag{3}$$

In order to improve the fidelity of the pressure integration, the original PIV mesh has been interpolated on a mesh with double the resolution, providing more accuracy to define the boundary conditions on the wing surface. During the interpolation the flow has been assumed to move with the wing speed at the wing surface to improve the near-wall estimate.

The loads on the wing have been computed by interpolating the pressure field over the airfoil surface and then computing the line integral according to the local normal direction of the surface.

The results have been compared to the measured loads in order to validate the pressure integration procedure. The results of the comparison have been reported in Fig. 1 for the case with $\theta_m = 10^\circ$ and $\theta_0 = 10^\circ$, showing that the pressure reconstruction is fairly accurate, especially in the lift component. Higher errors in the drag component are expected since viscous forces are not included in the Poisson approach.

3. Decomposition approach

The Proper Orthogonal Decomposition (POD, Berkooz et al. 1993) is a mathematical procedure which identifies a set of orthonormal eigenfunctions providing the most compact representation, in a least-square sense, of a set of observations. For the purposes of this work, let the observations correspond to the phase-averaged velocity fields measured with PIV at flapping phases, which leads to the bi-orthogonal POD definition (Aubry, 1991). The velocity field $\mathbf{u}(x,t)$ is approximated as:

$$\mathbf{u}(\mathbf{x},t) = \sum_{i=0}^{n_m} \psi^{(i)}(t)\sigma^{(i)}\phi^{(i)}(\mathbf{x}) \tag{4}$$

with $\mathbf{x}$, the spatial coordinate and t being the time coordinate. The set of functions $\phi^{(i)}(\mathbf{x})$ constitute the basis of the spatial decomposition of the fluctuating velocity field, $\psi^{(i)}(t)$ constitutes the basis of the temporal decomposition and $\sigma^{(i)}$ are the magnitudes associated to each mode; the symbol n_m indicates the number of modes. The choice of the eigenfunctions performed by the snapshot POD (Sirovich, 1987) aims at minimizing the projection residual of $\mathbf{u}(\mathbf{x},t)$ onto the set of functions $\psi^{(i)}(t)$ while constraining the set of $\psi^{(i)}(t)$ functions to be mutually orthogonal. The solution to this problem is given by the solution of the Fredholm equation, i.e. they are calculated as the eigenfunctions of the two-points temporal correlation tensor. It can be proven that the spatial basis $\phi^{(i)}(\mathbf{x})$, instead, are the eigenfunctions of the temporally-averaged spatial correlation operator. The singular values $\sigma^{(i)}$ are the square root of the correlation tensor eigenvalues and they measure the kinetic energy associated to each eigenfunction over the entire data ensemble. In the present work, it will be assumed that the time-averaged velocity field corresponds with $\psi^{(0)}(t)\sigma^{(0)}\phi^{(0)}(\mathbf{x})$ by construction, with $\psi^{(0)}(t)$ being constant in time.

The relation of the velocity modes with the pressure field can be determined from the Poisson equation (Eq. 2). Performing a Galerkin projection of such equation onto the space spanned by the velocity-based POD modes (see Eq. 5), it can be observed that the pressure depends quadratically from the velocity POD modes.

$$\begin{aligned} \nabla^2 p(\mathbf{x},t) &= -\rho \sum_{i=0}^{n_m}\sum_{j=0}^{n_m} \psi^{(i)}(t)\psi^{(j)}(t)\sigma^{(i)}\sigma^{(j)}Q^{(i,j)}(\mathbf{x}) \\ Q^{(i,j)}(\mathbf{x}) &= \nabla\cdot(\phi^{(\mathbf{i})}(\mathbf{x})\cdot\nabla)\phi^{(\mathbf{j})}(\mathbf{x}) \end{aligned} \tag{5}$$

It is worth noting that in Eq. 5 the terms having either $i = 0$ or $j = 0$ are necessarily linear in nature, since one of the time coefficients involved is constant in time (i.e. it stands for the time-average). While the POD-Galerkin projection can be used to directly assess the quadratic contribution of the velocity POD modes onto the pressure, this approach is complicated both by the necessity to restate the non-homogeneous Neumann boundary conditions in a matching quadratic form (see e.g. Noack et al., 2005) and by the fact that the Poisson equation should be solved in the wing-fixed reference frame which is not inertial. To overcome these complications, the quadratic relation has been captured using a Quadratic Stochastic Estimation (QSE). Following Ausseur et al. (2006), the QSE aims at solving the problem in Eq. 6 by minimizing the mean square error, with $\sigma_p^{(i,j)}$ and $P^{(i,j)}$ being the magnitude and the spatial distribution of the pressure field contribution correlated to the velocity-field mode pair $(\psi^{(i)}, \psi^{(j)})$.

$$p(\mathbf{x}, t) = \sum_{i=0}^{n_m} \sum_{j=0}^{n_m} \psi^{(i)}(t)\psi^{(j)}(t)\sigma_p^{(i,j)} P^{(i,j)}(\mathbf{x}) \tag{6}$$

The solution to this problem is provided by the solution of the matrix problem in Eq. 7, in which $P^{(i,j)}$ is the term to be solved and where $\langle\ ,\ \rangle$ indicates the inner product.

$$\begin{bmatrix} \langle \psi^{(1)}\psi^{(1)}, \psi^{(1)}\psi^{(1)} \rangle & \dots & \langle \psi^{(n_m)}\psi^{(n_m)}, \psi^{(1)}\psi^{(1)} \rangle \\ \vdots & \ddots & \vdots \\ \langle \psi^{(n_m)}\psi^{(n_m)}, \psi^{(1)}\psi^{(1)} \rangle & \dots & \langle \psi^{(n_m)}\psi^{(n_m)}, \psi^{(n_m)}\psi^{(n_m)} \rangle \end{bmatrix} \begin{bmatrix} P^{(1,1)} \\ \vdots \\ P^{(n_m,n_m)} \end{bmatrix} = \begin{bmatrix} \langle p, \psi^{(1)}\psi^{(1)} \rangle \\ \vdots \\ \langle p, \psi^{(n_m)}\psi^{(n_m)} \rangle \end{bmatrix} \tag{7}$$

In the present work the pressure contributions $P^{(i,j)}$ and $P^{(j,i)}$, correlated to the mode pairs $(\psi^{(i)}, \psi^{(j)})$ and $(\psi^{(j)}, \psi^{(i)})$, respectively, have been summed up and considered once, i.e. the contributions with $i < j$ have been set to zero.

4. Results and discussion

The results of the decomposition described in the previous section are here summarized for the flapping wing case with $\theta_m = 10°$ and $\theta_0 = 10°$. The POD of the velocity field is reported in Fig. 2 for the 0th mode (corresponding to the time average) to the 2nd mode. The contribution of these modes to the full field is reported in the following table, showing that these 3 modes recover more than 85% of the kinetic energy of the flow:

	$i = 0$	$i = 1$	$i = 2$
$\dfrac{\sigma^{(i)^2}}{\sum_i \sigma^{(i)^2}}$	32.3%	48.1%	6.7%

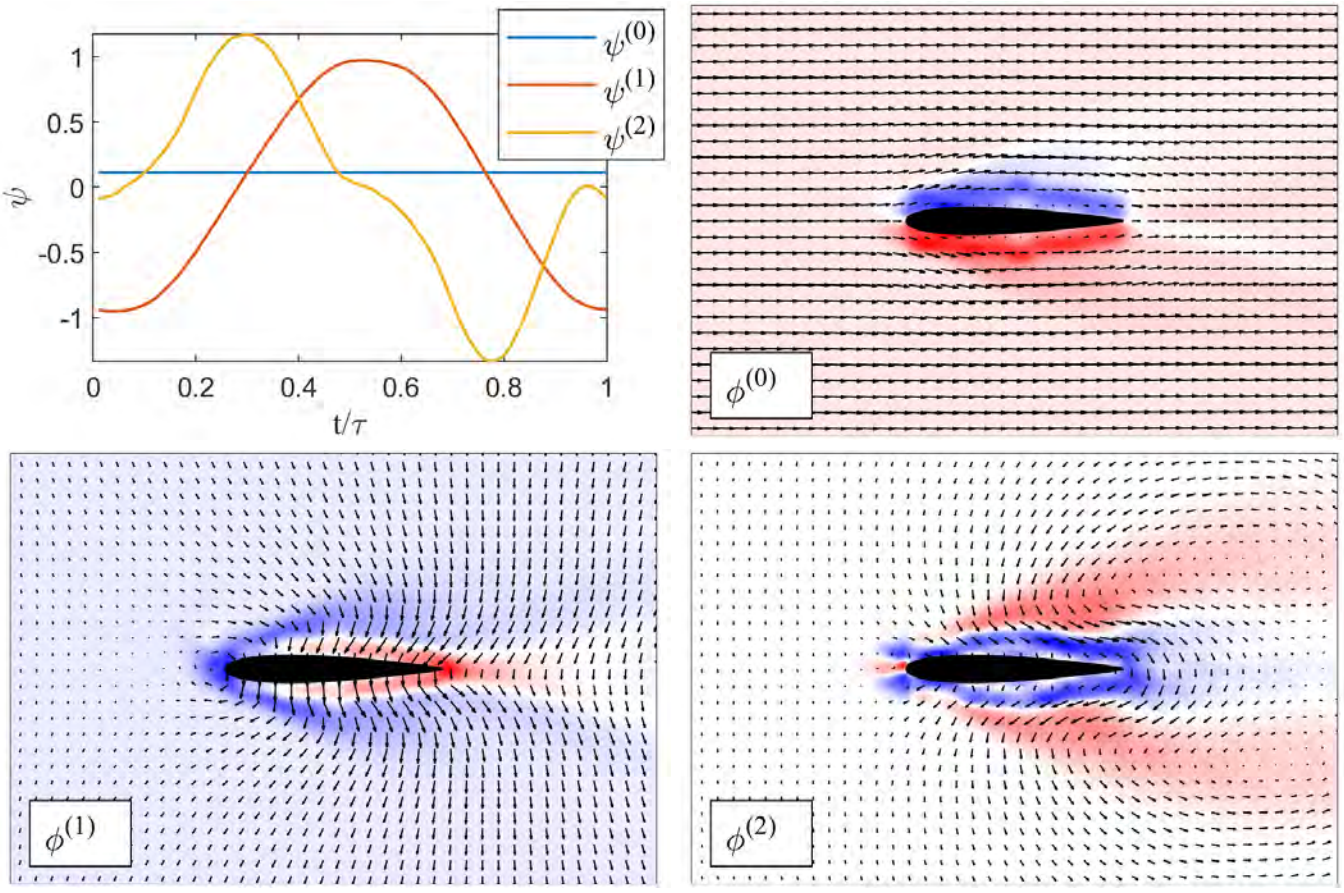

Figure 2. Proper Orthogonal Decomposition for the case with $\theta_m = 10^\circ$ and $\theta_0 = 10^\circ$: (top, left) POD temporal modes; (top, right) 0th POD spatial mode; (bottom, left) 1st POD spatial mode; (bottom, right) 2nd POD spatial mode. The spatial modes are represented in terms of vorticity (contour plot) and velocity (quiver plot).

The 0th mode represents a free-stream parallel to the wing chord and the boundary layer developing on top of the wing symmetrically. The 1st and 2nd mode represent vortical structures centered on the chord and localized at different chord-wise positions. Temporally, they show a sinusoidal behavior with a time shift of $\pi/2$ between them. When summed together accordingly to the POD decomposition in Eq. 4, they model the evolution of the quasi-steady bound vorticity on the wing, as well as the one due to LEV and TEV, during the flapping cycle (see Raiola et al., 2021).

Using these 3 modes, the QSE is performed to extract their contribution on the pressure field. The magnitude $\sigma_p^{(i,j)}$ of this contribution is shown Fig. 3, alongside to the magnitudes $\sigma_{F_y}^{(i,j)}$ and $\sigma_{F_x}^{(i,j)}$ of the contributions to the forces in the chord-normal and chord-wise directions, respectively, which results from the force computation from $\sigma_p^{(i,j)} P^{(i,j)}$. While all the mode pairs (i,j) contribute significantly to the pressure, with a slight dominance from the pairs (0,0) and (1,1), only few pairs contribute to the forces. In particular the chord-normal force is dominated by the contribution from the pair (0,1), with only a minor contribution from the pair (0,0) and (0,2), suggesting that the relation between the chord-normal force and the velocity field is mostly linear (all the pairs containing 0 are either constant in time or depending linearly on $\psi^{(i)}$). The chord-wise force, instead, is dominated by the constant contribution (0,0) and by the quadratic contribution (1,2).

The behavior reported in Fig. 3 is easily explained by the spatial distribution $P^{(i,j)}$ of the pressure contribution in Fig. 4. The contribution $P^{(0,1)}$ and $P^{(0,2)}$ arising from the interaction of the free-stream in mode 0th and the vortices in modes 1st and 2nd produce a pressure difference between the 2 sides of the wing, resulting in a chord-normal force. The time-constant contribution $P^{(0,0)}$ is mostly producing a pressure difference between leading and trailing edges of the wing (with a slight deflection which contributes to chord-normal force). Finally, the contribution $P^{(1,2)}$ arising from the mutual interaction of the vortical structures in modes 1st and 2nd produce a pressure difference between leading and trailing edges, resulting in a chord-wise force which oscillates with double the frequency of flapping.

Finally, the contributions of the pairs are reported in Fig. 5 in the order of their contribution to the related force components (on the left) as well as summed up in this same order (on the right). The force arising from the unprojected pressure in reported for comparison on the right, showing that the selected modes are enough to capture most of the force-related pressure field.

5. Conclusion

In this work the flow field around a flapping airfoil is measured by means of PIV. The velocity field is used to compute the pressure field by solving the 2D Poisson equation for pressure. The correctness of the pressure reconstruction is verified by means of comparison with the loads measured with a load cell. The velocity and pressure field obtained have been decomposed in the reference frame fixed with the wing in order to extract the flow features around the wing and their contribution to the pressure and loads. The velocity field is decomposed by means of POD. Based on the argument provided by the POD-Galerkin projection of the Poisson equation, the relation between

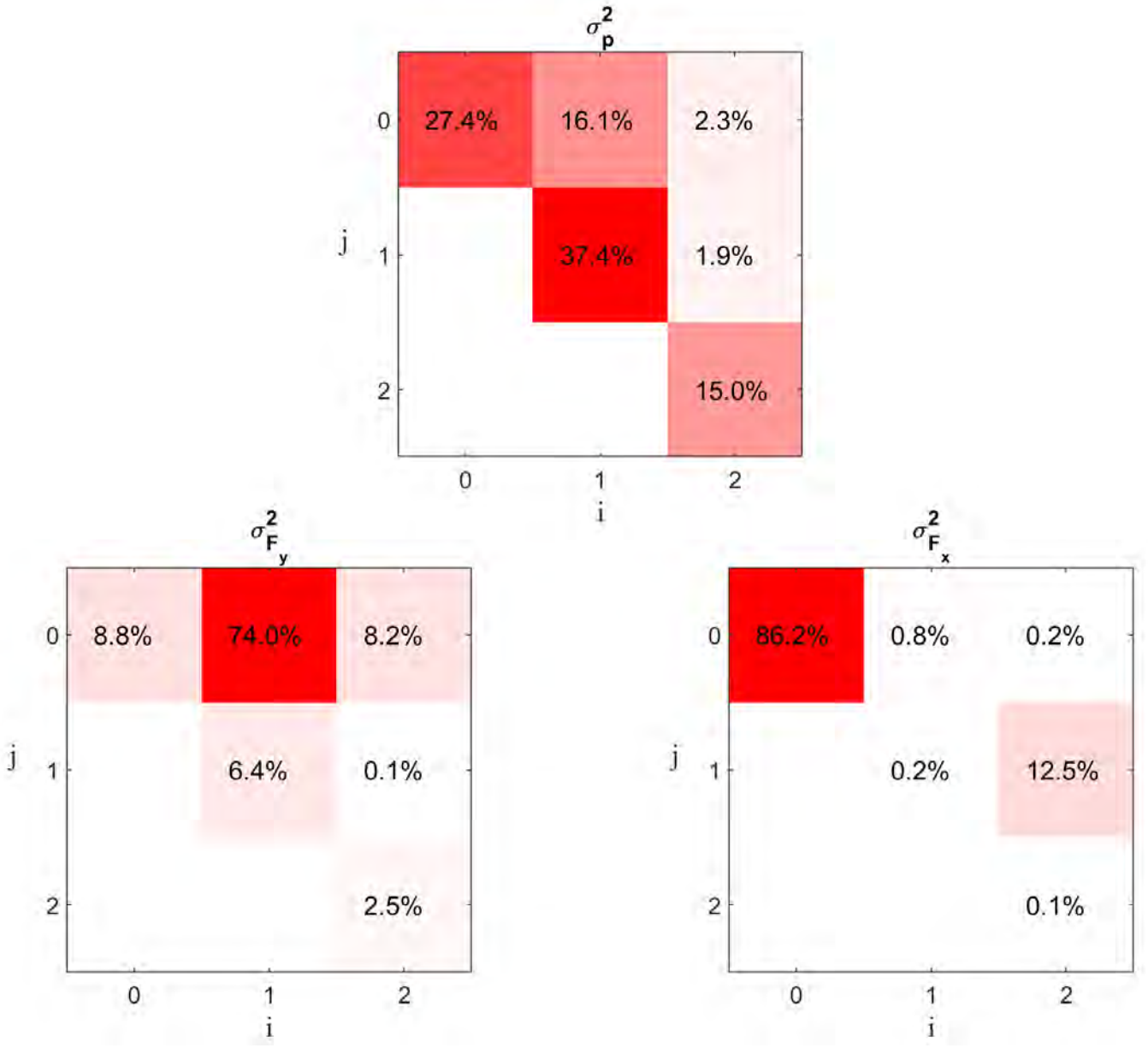

Figure 3. Squared magnitude of the contribution of the mode pair $(\psi^{(i)}, \psi^{(j)})$ to: (top) pressure σ_p^2; (bottom, left) chord-normal force $\sigma_{F_y}^2$; (bottom, right) chord-wise force $\sigma_{F_x}^2$. Results are indicated in terms of percentage of the total contribution of the first 3×3 modes.

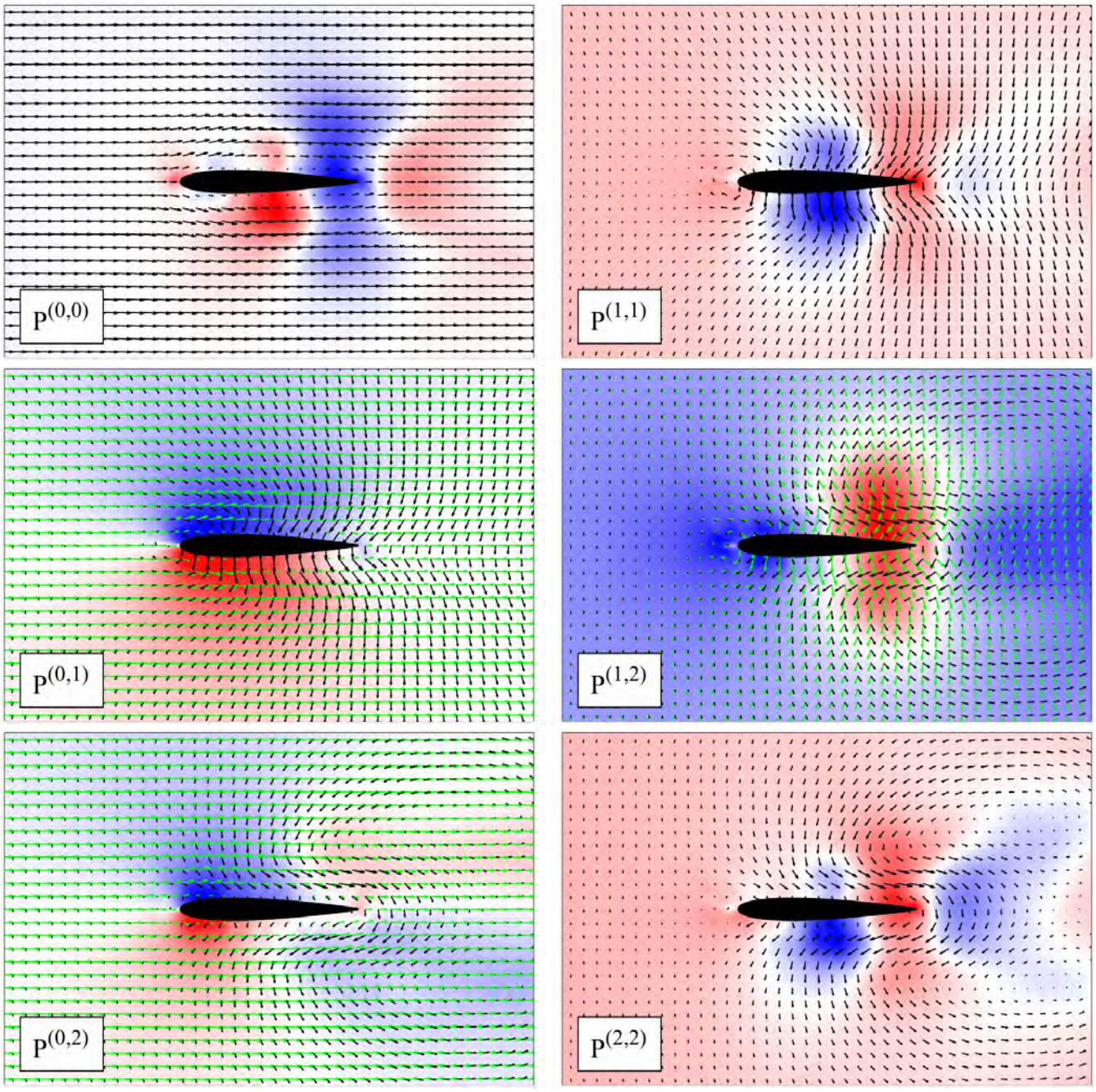

Figure 4. Spatial distribution $P^{(i,j)}$ of the contribution of the mode pair $(\psi^{(i)}, \psi^{(j)})$ to pressure for the modes from 0th to 2nd. The pressure distribution is reported in the colormap. Green and black quiver maps indicate the velocity field contained in the spatial POD modes $\phi^{(i)}$ and $\phi^{(j)}$, respectively.

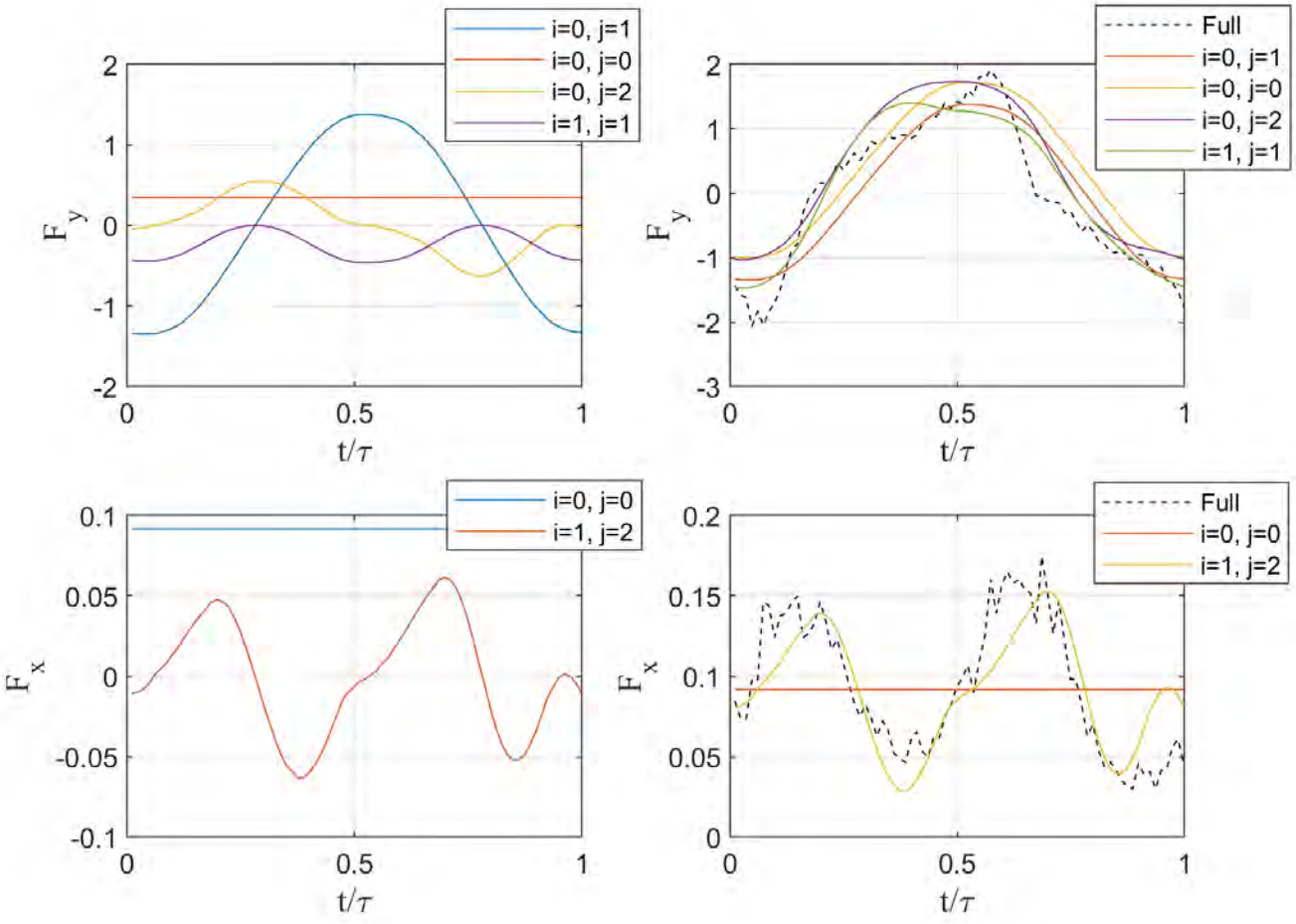

Figure 5. Force contribution computed from $\sigma_p^{(i,j)} P^{(i,j)}$: (left) force contribution from a single pair; (right) force contribution summing the most relevant pairs in order of importance. Plots on the top refer to the chord-normal force, plots on the bottom refer to the chord-wise force.

the velocity field modes and their pressure field contribution is assumed to be quadratic. This relation is extracted using a Quadratic Stochastic Estimation. The results of the decomposition reveal the presence of time-evolving vortical features on the wing (related to bound vorticity, LEV and TEV) which generate linearly-related chord-normal force by interacting with the free stream and quadratically-related chord-wise force fluctuations.

Acknowledgments

This work has been partially supported by grant PID2019-109717RB-I00 funded by the Spanish State Research Agency (SRA) and European Regional Development Fund (ERDF).

References

Aubry, N. (1991). On the hidden beauty of the proper orthogonal decomposition. *Theoretical and Computational Fluid Dynamics*, *2*(5-6), 339–352.

Ausseur, J., Pinier, J., Glauser, M., Higuchi, H., & Carlson, H. (2006). Experimental development of a reduced order model for flow sepapration control. In *44th aiaa aerospace sciences meeting and exhibit* (p. 1251).

Baars, W. J., & Tinney, C. E. (2014). Proper orthogonal decomposition-based spectral higher-order stochastic estimation. *Physics of Fluids*, *26*(5), 055112.

Berkooz, G., Holmes, P., & Lumley, J. L. (1993). The proper orthogonal decomposition in the analysis of turbulent flows. *Annual Review of Fluid Mechanics*, *25*(1), 539–575.

Borée, J. (2003). Extended proper orthogonal decomposition: a tool to analyse correlated events in turbulent flows. *Experiments in Fluids*, *35*(2), 188–192.

Brunton, S. L., Rowley, C. W., & Williams, D. R. (2013). Reduced-order unsteady aerodynamic models at low Reynolds numbers. *Journal of Fluid Mechanics*, *724*, 203–233.

Ellington, C. P. (1984). The aerodynamics of hovering insect flight. IV. Aerodynamic mechanisms. *Philosophical Transactions of the Royal Society of London B: Biological Sciences*, *305*(1122), 79–113.

Garrick, I. E. (1937). Propulsion of a flapping and oscillating airfoil. *NACA Report 567*.

Lewin, G. C., & Haj-Hariri, H. (2005). Reduced-order modeling of a heaving airfoil. *AIAA Journal*, *43*(2), 270–283.

Liang, Z., & Dong, H. (2015). On the symmetry of proper orthogonal decomposition modes of a low-aspect-ratio plate. *Physics of Fluids*, *27*(6), 063601.

Lighthill, M. J. (1969). Hydromechanics of aquatic animal propulsion. *Annual Review of Fluid Mechanics*, *1*(1), 413–446.

Mendez, M. A., Raiola, M., Masullo, A., Discetti, S., Ianiro, A., Theunissen, R., & Buchlin, J.-M. (2017). POD-based background removal for particle image velocimetry. *Experimental Thermal and Fluid Science*, *80*, 181–192.

Naguib, A., Wark, C., & Juckenhöfel, O. (2001). Stochastic estimation and flow sources associated with surface pressure events in a turbulent boundary layer. *Physics of Fluids*, *13*(9), 2611–2626.

Noack, B. R., Papas, P., & Monkewitz, P. A. (2005). The need for a pressure-term representation in empirical galerkin models of incompressible shear flows. *Journal of Fluid Mechanics*, *523*, 339–365.

Noca, F., Shiels, D., & Jeon, D. (1999). A comparison of methods for evaluating time-dependent fluid dynamic forces on bodies, using only velocity fields and their derivatives. *Journal of Fluids and Structures*, *13*(5), 551–578.

Pesavento, U., & Wang, Z. J. (2004). Falling paper: Navier-Stokes solutions, model of fluid forces, and center of mass elevation. *Physical Review Letters*, *93*(14), 144501.

Raiola, M., Discetti, S., & Ianiro, A. (2021). Data-driven identification of unsteady-aerodynamics phenomena in flapping airfoils. *Experimental Thermal and Fluid Science*, *124*, 110234.

Reimer, A. S., & Cheviakov, A. F. (2013). A matlab-based finite-difference solver for the poisson problem with mixed dirichlet–neumann boundary conditions. *Computer Physics Communications*, *184*(3), 783–798.

Sane, S. P., & Dickinson, M. H. (2002). The aerodynamic effects of wing rotation and a revised quasi-steady model of flapping flight. *Journal of Experimental Biology*, *205*(8), 1087–1096.

Scarano, F. (2001). Iterative image deformation methods in PIV. *Measurement Science and Technology*, *13*(1), R1.

Shyy, W., Lian, Y., Tang, J., Viieru, D., & Liu, H. (2007). *Aerodynamics of low reynolds number flyers*. Cambridge University Press.

Sirovich, L. (1987). Turbulence and the dynamics of coherent structures. Part I: Coherent structures. *Quarterly of Applied Mathematics*, *45*(3), 561–571.

Theodorsen, T. (1935). General theory of aerodynamic instability and the mechanism of flutter. *NACA Report 496*.

Troshin, V., & Seifert, A. (2018). Modeling of a pitching and plunging airfoil using experimental flow field and load measurements. *Experiments in Fluids*, *59*(1), 6.

Van Oudheusden, B. (2013). PIV-based pressure measurement. *Measurement Science and Technology*, *24*(3), 032001.

Westerweel, J. (1997). Fundamentals of digital particle image velocimetry. *Measurement Science and Technology*, *8*, 1379–92.